Search for High Frequency Gravitational Wave Bursts in the First Calendar Year of LIGO's Fifth Science Run

B. P. Abbott,[17] R. Abbott,[17] R. Adhikari,[17] P. Ajith,[2] B. Allen,[2,60] G. Allen,[35] R. S. Amin,[21] S. B. Anderson,[17] W. G. Anderson,[60] M. A. Arain,[47] M. Araya,[17] H. Armandula,[17] P. Armor,[60] Y. Aso,[17] S. Aston,[46] P. Aufmuth,[16] C. Aulbert,[2] S. Babak,[1] P. Baker,[24] S. Ballmer,[17] C. Barker,[18] D. Barker,[18] B. Barr,[48] P. Barriga,[59] L. Barsotti,[20] M. A. Barton,[17] I. Bartos,[10] R. Bassiri,[48] M. Bastarrika,[48] B. Behnke,[1] M. Benacquista,[42] J. Betzwieser,[17] P. T. Beyersdorf,[31] I. A. Bilenko,[25] G. Billingsley,[17] R. Biswas,[60] E. Black,[17] J. K. Blackburn,[17] L. Blackburn,[20] D. Blair,[59] B. Bland,[18] T. P. Bodiya,[20] L. Bogue,[19] R. Bork,[17] V. Boschi,[17] S. Bose,[61] P. R. Brady,[60] V. B. Braginsky,[25] J. E. Brau,[53] D. O. Bridges,[19] M. Brinkmann,[2] A. F. Brooks,[17] D. A. Brown,[36] A. Brummit,[30] G. Brunet,[20] A. Bullington,[35] A. Buonanno,[49] O. Burmeister,[2] R. L. Byer,[35] L. Cadonati,[50] J. B. Camp,[26] J. Cannizzo,[26] K. C. Cannon,[17] J. Cao,[20] L. Cardenas,[17] S. Caride,[51] G. Castaldi,[56] S. Caudill,[21] M. Cavaglià,[39] C. Cepeda,[17] T. Chalermsongsak,[17] E. Chalkley,[48] P. Charlton,[9] S. Chatterji,[17] S. Chelkowski,[46] Y. Chen,[1,6] N. Christensen,[8] C. T. Y. Chung,[38] D. Clark,[35] J. Clark,[7] J. H. Clayton,[60] T. Cokelaer,[7] C. N. Colacino,[12] R. Conte,[55] D. Cook,[18] T. R. C. Corbitt,[20] N. Cornish,[24] D. Coward,[59] D. C. Coyne,[17] A. Di Credico,[36] J. D. E. Creighton,[60] T. D. Creighton,[42] A. M. Cruise,[46] R. M. Culter,[46] A. Cumming,[48] L. Cunningham,[48] S. L. Danilishin,[25] K. Danzmann,[2,16] B. Daudert,[17] G. Davies,[7] E. J. Daw,[40] D. DeBra,[35] J. Degallaix,[2] V. Dergachev,[51] S. Desai,[37] R. DeSalvo,[17] S. Dhurandhar,[15] M. Díaz,[42] A. Dietz,[7] F. Donovan,[20] K. L. Dooley,[47] E. E. Doomes,[34] R. W. P. Drever,[5] J. Dueck,[2] I. Duke,[20] J. -C. Dumas,[59] J. G. Dwyer,[10] C. Echols,[17] M. Edgar,[48] A. Effler,[18] P. Ehrens,[17] E. Espinoza,[17] T. Etzel,[17] M. Evans,[20] T. Evans,[19] S. Fairhurst,[7] Y. Faltas,[47] Y. Fan,[59] D. Fazi,[17] H. Fehrmann,[2] L. S. Finn,[37] K. Flasch,[60] S. Foley,[20] C. Forrest,[54] N. Fotopoulos,[60] A. Franzen,[16] M. Frede,[2] M. Frei,[41] Z. Frei,[12] A. Freise,[46] R. Frey,[53] T. Fricke,[19] P. Fritschel,[20] V. V. Frolov,[19] M. Fyffe,[19] V. Galdi,[56] J. A. Garofoli,[36] I. Gholami,[1] J. A. Giaime,[21,19] S. Giampanis,[2] K. D. Giardina,[19] K. Goda,[20] E. Goetz,[51] L. M. Goggin,[60] G. González,[21] M. L. Gorodetsky,[25] S. Goßler,[2] R. Gouaty,[21] A. Grant,[48] S. Gras,[59] C. Gray,[18] M. Gray,[4] R. J. S. Greenhalgh,[30] A. M. Gretarsson,[11] F. Grimaldi,[20] R. Grosso,[42] H. Grote,[2] S. Grunewald,[1] M. Guenther,[18] E. K. Gustafson,[17] R. Gustafson,[51] B. Hage,[16] J. M. Hallam,[46] D. Hammer,[60] G. D. Hammond,[48] C. Hanna,[17] J. Hanson,[19] J. Harms,[52] G. M. Harry,[20] I. W. Harry,[7] E. D. Harstad,[53] K. Haughian,[48] K. Hayama,[42] J. Heefner,[17] I. S. Heng,[48] A. Heptonstall,[17] M. Hewitson,[2] S. Hild,[46] E. Hirose,[36] D. Hoak,[19] K. A. Hodge,[17] K. Holt,[19] D. J. Hosken,[45] J. Hough,[48] D. Hoyland,[59] B. Hughey,[20] S. H. Huttner,[48] D. R. Ingram,[18] T. Isogai,[8] M. Ito,[53] A. Ivanov,[17] B. Johnson,[18] W. W. Johnson,[21] D. I. Jones,[57] G. Jones,[7] R. Jones,[48] L. Ju,[59] P. Kalmus,[17] V. Kalogera,[28] S. Kandhasamy,[52] J. Kanner,[49] D. Kasprzyk,[46] E. Katsavounidis,[20] K. Kawabe,[18] S. Kawamura,[27] F. Kawazoe,[2] W. Kells,[17] D. G. Keppel,[17] A. Khalaidovski,[2] F. Y. Khalili,[25] R. Khan,[10] E. Khazanov,[14] P. King,[17] J. S. Kissel,[21] S. Klimenko,[47] K. Kokeyama,[27] V. Kondrashov,[17] R. Kopparapu,[37] S. Koranda,[60] D. Kozak,[17] B. Krishnan,[1] R. Kumar,[48] P. Kwee,[16] P. K. Lam,[4] M. Landry,[18] B. Lantz,[35] A. Lazzarini,[17] H. Lei,[42] M. Lei,[17] N. Leindecker,[35] I. Leonor,[53] C. Li,[6] H. Lin,[47] P. E. Lindquist,[17] T. B. Littenberg,[24] N. A. Lockerbie,[58] D. Lodhia,[46] M. Longo,[56] M. Lormand,[19] P. Lu,[35] M. Lubinski,[18] A. Lucianetti,[47] H. Lück,[2,16] B. Machenschalk,[1] M. MacInnis,[20] M. Mageswaran,[17] K. Mailand,[17] I. Mandel,[28] V. Mandic,[52] S. Márka,[10] Z. Márka,[10] A. Markosyan,[35] J. Markowitz,[20] E. Maros,[17] I. W. Martin,[48] R. M. Martin,[47] J. N. Marx,[17] K. Mason,[20] F. Matichard,[21] L. Matone,[10] R. A. Matzner,[41] N. Mavalvala,[20] R. McCarthy,[18] D. E. McClelland,[4] S. C. McGuire,[34] M. McHugh,[23] G. McIntyre,[17] D. J. A. McKechan,[7] K. McKenzie,[4] M. Mehmet,[2] A. Melatos,[38] A. C. Melissinos,[54] D. F. Menéndez,[37] G. Mendell,[18] R. A. Mercer,[60] S. Meshkov,[17] C. Messenger,[2] M. S. Meyer,[19] J. Miller,[48] J. Minelli,[37] Y. Mino,[6] V. P. Mitrofanov,[25] G. Mitselmakher,[47] R. Mittleman,[20] O. Miyakawa,[17] B. Moe,[60] S. D. Mohanty,[42] S. R. P. Mohapatra,[50] G. Moreno,[18] T. Morioka,[27] K. Mors,[2] K. Mossavi,[2] C. MowLowry,[4] G. Mueller,[47] H. Müller-Ebhardt,[2] D. Muhammad,[19] S. Mukherjee,[42] H. Mukhopadhyay,[15] A. Mullavey,[4] J. Munch,[45] P. G. Murray,[48] E. Myers,[18] J. Myers,[18] T. Nash,[17] J. Nelson,[48] G. Newton,[48] A. Nishizawa,[27] K. Numata,[26] J. O'Dell,[30] B. O'Reilly,[19] R. O'Shaughnessy,[37] E. Ochsner,[49] G. H. Ogin,[17] D. J. Ottaway,[45] R. S. Ottens,[47] H. Overmier,[19] B. J. Owen,[37] Y. Pan,[49] C. Pankow,[47] M. A. Papa,[1,60] V. Parameshwaraiah,[18] P. Patel,[17] M. Pedraza,[17] S. Penn,[13] A. Perraca,[46] V. Pierro,[56] I. M. Pinto,[56] M. Pitkin,[48] H. J. Pletsch,[2] M. V. Plissi,[48] F. Postiglione,[55] M. Principe,[56] R. Prix,[2] L. Prokhorov,[25] O. Punken,[2] V. Quetschke,[47] F. J. Raab,[18] D. S. Rabeling,[4] H. Radkins,[18] P. Raffai,[12] Z. Raics,[10] N. Rainer,[2] M. Rakhmanov,[42] V. Raymond,[28] C. M. Reed,[18] T. Reed,[22] H. Rehbein,[2] S. Reid,[48] D. H. Reitze,[47] R. Riesen,[19] K. Riles,[51] B. Rivera,[18] P. Roberts,[3] N. A. Robertson,[17,48] C. Robinson,[7] E. L. Robinson,[1] S. Roddy,[19] C. Röver,[2] J. Rollins,[10] J. D. Romano,[42] J. H. Romie,[19] S. Rowan,[48] A. Rüdiger,[2] P. Russell,[17] K. Ryan,[18] S. Sakata,[27] L. Sancho de la Jordana,[44] V. Sandberg,[18] V. Sannibale,[17] L. Santamaría,[1] S. Saraf,[32] P. Sarin,[20] B. S. Sathyaprakash,[7] S. Sato,[27] M. Satterthwaite,[4] P. R. Saulson,[36] R. Savage,[18] P. Savov,[6] M. Scanlan,[22] R. Schilling,[2] R. Schnabel,[2] R. Schofield,[53] B. Schulz,[2] B. F. Schutz,[1,7] P. Schwinberg,[18] J. Scott,[48] S. M. Scott,[4] A. C. Searle,[17] B. Sears,[17] F. Seifert,[2] D. Sellers,[19] A. S. Sengupta,[17] A. Sergeev,[14] B. Shapiro,[20] P. Shawhan,[49] D. H. Shoemaker,[20] A. Sibley,[19] X. Siemens,[60] D. Sigg,[18] S. Sinha,[35] A. M. Sintes,[44] B. J. J. Slagmolen,[4] J. Slutsky,[21] J. R. Smith,[36] M. R. Smith,[17] N. D. Smith,[20] K. Somiya,[6] B. Sorazu,[48] A. Stein,[20] L. C. Stein,[20] S. Steplewski,[61]

A. Stochino,[17] R. Stone,[42] K. A. Strain,[48] S. Strigin,[25] A. Stroeer,[26] A. L. Stuver,[19] T. Z. Summerscales,[3] K. -X. Sun,[35] M. Sung,[21] P. J. Sutton,[7] G. P. Szokoly,[12] D. Talukder,[61] L. Tang,[42] D. B. Tanner,[47] S. P. Tarabrin,[25] J. R. Taylor,[2] R. Taylor,[17] J. Thacker,[19] K. A. Thorne,[19] K. S. Thorne,[6] A. Thüring,[16] K. V. Tokmakov,[48] C. Torres,[19] C. Torrie,[17] G. Traylor,[19] M. Trias,[44] D. Ugolini,[43] J. Ulmen,[35] K. Urbanek,[35] H. Vahlbruch,[16] M. Vallisneri,[6] C. Van Den Broeck,[7] M. V. van der Sluys,[28] A. A. van Veggel,[48] S. Vass,[17] R. Vaulin,[60] A. Vecchio,[46] J. Veitch,[46] P. Veitch,[45] C. Veltkamp,[2] J. Villadsen,[20] A. Villar,[17] C. Vorvick,[18] S. P. Vyachanin,[25] S. J. Waldman,[20] L. Wallace,[17] R. L. Ward,[17] A. Weidner,[2] M. Weinert,[2] A. J. Weinstein,[17] R. Weiss,[20] L. Wen,[6,59] S. Wen,[21] K. Wette,[4] J. T. Whelan,[1,29] S. E. Whitcomb,[17] B. F. Whiting,[47] C. Wilkinson,[18] P. A. Willems,[17] H. R. Williams,[37] L. Williams,[47] B. Willke,[2,16] I. Wilmut,[30] L. Winkelmann,[2] W. Winkler,[2] C. C. Wipf,[20] A. G. Wiseman,[60] G. Woan,[48] R. Wooley,[19] J. Worden,[18] W. Wu,[47] I. Yakushin,[19] H. Yamamoto,[17] Z. Yan,[59] S. Yoshida,[33] M. Zanolin,[11] J. Zhang,[51] L. Zhang,[17] C. Zhao,[59] N. Zotov,[22] M. E. Zucker,[20] H. zur Mühlen,[16] and J. Zweizig[17]

(The LIGO Scientific Collaboration, http://www.ligo.org)

[1]*Albert-Einstein-Institut, Max-Planck-Institut für Gravitationsphysik, D-14476 Golm, Germany*
[2]*Albert-Einstein-Institut, Max-Planck-Institut für Gravitationsphysik, D-30167 Hannover, Germany*
[3]*Andrews University, Berrien Springs, MI 49104 USA*
[4]*Australian National University, Canberra, 0200, Australia*
[5]*California Institute of Technology, Pasadena, CA 91125, USA*
[6]*Caltech-CaRT, Pasadena, CA 91125, USA*
[7]*Cardiff University, Cardiff, CF24 3AA, United Kingdom*
[8]*Carleton College, Northfield, MN 55057, USA*
[9]*Charles Sturt University, Wagga Wagga, NSW 2678, Australia*
[10]*Columbia University, New York, NY 10027, USA*
[11]*Embry-Riddle Aeronautical University, Prescott, AZ 86301 USA*
[12]*Eötvös University, ELTE 1053 Budapest, Hungary*
[13]*Hobart and William Smith Colleges, Geneva, NY 14456, USA*
[14]*Institute of Applied Physics, Nizhny Novgorod, 603950, Russia*
[15]*Inter-University Centre for Astronomy and Astrophysics, Pune - 411007, India*
[16]*Leibniz Universität Hannover, D-30167 Hannover, Germany*
[17]*LIGO - California Institute of Technology, Pasadena, CA 91125, USA*
[18]*LIGO - Hanford Observatory, Richland, WA 99352, USA*
[19]*LIGO - Livingston Observatory, Livingston, LA 70754, USA*
[20]*LIGO - Massachusetts Institute of Technology, Cambridge, MA 02139, USA*
[21]*Louisiana State University, Baton Rouge, LA 70803, USA*
[22]*Louisiana Tech University, Ruston, LA 71272, USA*
[23]*Loyola University, New Orleans, LA 70118, USA*
[24]*Montana State University, Bozeman, MT 59717, USA*
[25]*Moscow State University, Moscow, 119992, Russia*
[26]*NASA/Goddard Space Flight Center, Greenbelt, MD 20771, USA*
[27]*National Astronomical Observatory of Japan, Tokyo 181-8588, Japan*
[28]*Northwestern University, Evanston, IL 60208, USA*
[29]*Rochester Institute of Technology, Rochester, NY 14623, USA*
[30]*Rutherford Appleton Laboratory, HSIC, Chilton, Didcot, Oxon OX11 0QX United Kingdom*
[31]*San Jose State University, San Jose, CA 95192, USA*
[32]*Sonoma State University, Rohnert Park, CA 94928, USA*
[33]*Southeastern Louisiana University, Hammond, LA 70402, USA*
[34]*Southern University and A&M College, Baton Rouge, LA 70813, USA*
[35]*Stanford University, Stanford, CA 94305, USA*
[36]*Syracuse University, Syracuse, NY 13244, USA*
[37]*The Pennsylvania State University, University Park, PA 16802, USA*
[38]*The University of Melbourne, Parkville VIC 3010, Australia*
[39]*The University of Mississippi, University, MS 38677, USA*
[40]*The University of Sheffield, Sheffield S10 2TN, United Kingdom*
[41]*The University of Texas at Austin, Austin, TX 78712, USA*
[42]*The University of Texas at Brownsville and Texas Southmost College, Brownsville, TX 78520, USA*
[43]*Trinity University, San Antonio, TX 78212, USA*
[44]*Universitat de les Illes Balears, E-07122 Palma de Mallorca, Spain*
[45]*University of Adelaide, Adelaide, SA 5005, Australia*
[46]*University of Birmingham, Birmingham, B15 2TT, United Kingdom*
[47]*University of Florida, Gainesville, FL 32611, USA*
[48]*University of Glasgow, Glasgow, G12 8QQ, United Kingdom*
[49]*University of Maryland, College Park, MD 20742 USA*
[50]*University of Massachusetts - Amherst, Amherst, MA 01003, USA*

[51]University of Michigan, Ann Arbor, MI 48109, USA
[52]University of Minnesota, Minneapolis, MN 55455, USA
[53]University of Oregon, Eugene, OR 97403, USA
[54]University of Rochester, Rochester, NY 14627, USA
[55]University of Salerno, 84084 Fisciano (Salerno), Italy
[56]University of Sannio at Benevento, I-82100 Benevento, Italy
[57]University of Southampton, Southampton, SO17 1BJ, United Kingdom
[58]University of Strathclyde, Glasgow, G1 1XQ, United Kingdom
[59]University of Western Australia, Crawley, WA 6009, Australia
[60]University of Wisconsin-Milwaukee, Milwaukee, WI 53201, USA
[61]Washington State University, Pullman, WA 99164, USA

We present an all-sky search for gravitational waves in the frequency range 1 to 6 kHz during the first calendar year of LIGO's fifth science run. This is the first untriggered LIGO burst analysis to be conducted above 3 kHz. We discuss the unique properties of interferometric data in this regime. 161.3 days of triple-coincident data were analyzed. No gravitational events above threshold were observed and a frequentist upper limit of 5.4 year^{-1} on the rate of strong gravitational wave bursts was placed at a 90% confidence level. Implications for specific theoretical models of gravitational wave emission are also discussed.

PACS numbers:

I. INTRODUCTION

LIGO (Laser Interferometer Gravitational Wave Observatory) [1] is composed of three laser interferometers at two sites in the United States of America. The interferometers known as H1, with 4 km arms, and H2, with 2 km arms, are colocated within the same vacuum system at the Hanford site in Washington state. An additional 4-kilometer-long interferometer, L1, is located in Louisiana's Livingston Parish. The detectors have similar orientation, as far as is possible given the curvature of the Earth's surface and the constraints of the sites on which they were built, in order to be sensitive to the same gravitational wave polarizations. The relatively large separation between the two sites (approximately 3000 km) helps distinguish an actual gravitational wave appearing in both detectors from local environmental disturbances, which should not have a corresponding signal at the other site. GEO 600, a 600 m interferometer located near Hannover Germany, also operates as part of the LIGO Scientific Collaboration.

The fifth science run (S5) of the LIGO interferometers was conducted between November 2005 and October 2007. LIGO achieved its design sensitivity during this run, roughly a factor of 2 improvement in sensitivity over the previous S4 run [2]. Additionally, S5 was by far the longest science run and had the best duty cycle, collecting a full year of livetime of data with all 3 LIGO detectors in science mode. This is an order of magnitude greater triple-coincident livetime than all previous LIGO science runs combined. The analysis discussed in this paper uses data from the first calendar year of S5, covering data from 4 November 2005 to 14 November 2006.

Previous all-sky searches for bursts of gravitational waves with LSC instruments have been limited to frequencies below 3 kHz or less, in the range where the detectors are maximally sensitive [2, 3, 4, 5, 6]. The sensitivity above 1 kHz is poorer than at lower frequencies because of the storage time limit of the interferometer arms, as demonstrated by the strain-equivalent noise spectral density curve for H1, H2 and L1 shown in Figure 1. Shot noise (random statistical fluctuations in the number of photons hitting the photodetector) is the dominant source of noise above $\sim$200 Hz.

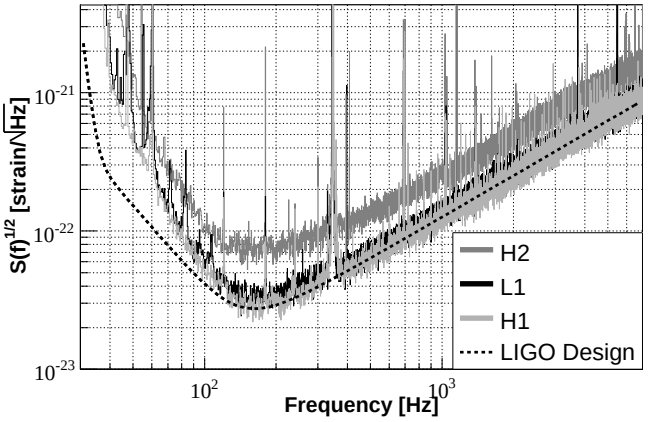

FIG. 1: Characteristic LIGO sensitivity curves from early in the S5 run. The sensitivity improved from February 2006 onward. Shot noise dominates the spectrum at high frequencies.

Despite the higher noise floor, the interferometers are still sensitive enough to merit analysis in the few kilohertz regime and there are a number of models which lead to gravitational wave emission above 2 kHz. As the sensitivity of gravitational wave interferometers continues to improve, it is important to explore the full range of data produced by them. LIGO samples data at 16384 Hz, in principle allowing analysis up to 8192 Hz, but the data are not calibrated up to the Nyquist frequency. Thus, this paper describes an all-sky high frequency search for gravitational burst signals using H1, H2 and L1 data in triple coincidence in the frequency range 1–6 kHz. This search complements the all-sky burst search in the 64 Hz–2 kHz range, described in [19].

This paper is organized as follows: Section II describes the theoretical motivation for conducting this search. Section III

describes the analysis procedure. Section IV discusses general properties of high frequency data and systematic uncertainties. Section V discusses detection efficiencies based on simulated waveforms. Results are presented in section VI, followed by discussion and summary in section VII.

II. TRANSIENT SOURCES OF FEW-KHZ GRAVITATIONAL WAVES

A number of specific theoretical models predict transient gravitational wave emission in the few-kilohertz range. One such potential source of emission is gravitational collapse, including core-collapse supernova and long-soft gamma-ray burst scenarios [7] which are predicted to emit gravitational waves in a range extending above 1 kHz. In a somewhat higher frequency regime are neutron star collapse scenarios resulting in rotating black holes [8, 9].

Another potential class of high frequency gravitational wave sources is nonaxisymmetric hypermassive neutron stars resulting from neutron star-neutron star mergers. If the equation of state is sufficiently stiff, a hypermassive neutron star is formed as an intermediate step during the merger of two neutron stars before a final collapse to a black hole, whereas a softer equation of state leads to prompt formation of a black hole. Some models predict gravitational wave emission in the 2–4 kHz range from this intermediate hypermassive neutron star, but much higher frequency emission (6–7 kHz) from a promptly formed black hole [10]. Observation of few-kilohertz gravitational wave emission from such systems would thus provide information about the equation of state of the system being studied.

Other possible sources of few-kilohertz gravitational wave emission include neutron star normal modes (in particular the f-mode) [11] as well as neutron stars undergoing torque-free precession as a result of accreting matter from a binary companion [12]. Low-mass black hole mergers [13], soft gamma repeaters [14] or some scenarios for gravitational emission from cosmic string cusps [15] are additional possible sources. The majority of predicted high frequency gravitational wave signals tend to be of a few cycles duration in most scenarios since strong signals tend to lead to strong backreactions and hence significant damping.

While there are specific waveform predictions from many of these models (some of which are studied in this analysis) these models still have substantial uncertainties and are only valid for systems with very specific sets of properties (e.g. mass and spin). Thus, as has been done previously for lower frequencies in each science run, we use search techniques that do not make use of specific waveforms. We require only short ($\ll$1 s) duration and substantial signal power in the analysis band.

III. DATA ANALYSIS

The process of identifying potential gravitational wave candidate events and separating them from noise fluctuations and instrumental glitches takes place in several steps. A schematic outline of the analysis pipeline is shown in Fig. 2. Using whitened data, triggers with frequency above 1kHz are identified separately at the two LIGO sites using the QPipeline algorithm [17, 18, 19], then combined with triggers of consistent time and frequency at the other site in the post-processing stage. The data quality cuts and veto stages remove triggers correlated with instrumental and environmental disturbances that are known to be not of gravitational wave origin. Remaining triggers are then subjected to a final cut based on the consistency of the signal shape in the three interferometers [22]. The analysis procedure is described in greater detail in the remainder of this section.

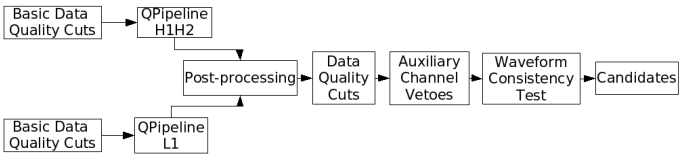

FIG. 2: A schematic of the analysis pipeline. *Triggers*, which are times when the power in one or more interferometer's readout is in excess of the baseline noise, are generated using the QPipeline algorithm [17, 18, 19]. Post-processing includes checking for a corresponding trigger at the other site and clustering remaining triggers into 1 second periods to avoid multiple triggers from the same source. Data quality cuts remove triggers from times with known disturbances which can contaminate the data with spurious transients of mundane origin. The remaining triggers are subjected to auxiliary channel vetoes and finally a waveform consistency test is performed using CorrPower [22].

These procedures were developed using time-shifted data produced by sliding the time stamps of Livingston triggers relative to Hanford triggers with 100 different time-shifts in increments of 5 seconds. Applying multiple time-shifts allows us to produce a set of independent time-shifted triggers with an effective livetime much larger than the actual livetime of the analysis. Since 5 seconds is much longer than the light travel time between the detectors, even after padding for the finite time resolution of our search, no genuine gravitational wave signals will be coincident with themselves in the time-shifted data streams, allowing us to use this set of time-shifted triggers as background data. H1 and H2 data streams are not shifted relative to each other because their common environment is likely to produce temporally correlated non-stationary noise, meaning that time-shifts between H1 and H2 would not accurately represent real background. The analysis was tested on a single day of data (December 11th, 2005), then extended to the entire first calendar year of S5.

GEO 600, a 600 meter interferometer in Germany, was also collecting gravitational wave data during this timeframe. However, since the smaller GEO 600 interferometer is substantially less sensitive than LIGO, including GEO 600 would not have caused a substantial increase in overall sensitivity. Also, incorporating an additional interferometer not co-aligned with the others would have added substantial complications to the analysis, especially since the cross-correlation

test we perform with CorrPower [22] is not designed to analyze data from detectors that are misaligned. Thus, for this analysis, we used GEO 600 data as a follow-up only, to be examined in the case that any event candidates were identified using LIGO. Virgo [16], a 3 km interferometer located in Cascina, Italy, was not operating during the period described in this paper. Joint analysis of LIGO and Virgo data at high frequencies will be described in a future publication.

A. The QPipeline Algorithm

The QPipeline algorithm is run on calibrated strain data [20] to identify triggers. Each trigger is identified by a central time, duration, central frequency, bandwidth and normalized energy. Any trigger surviving to the end of the pipeline described in Figure 2 would be considered as a gravitational wave candidate event. However, the vast majority of triggers generated by QPipeline are of mundane origin.

Before searching for triggers, QPipeline whitens the data using zero-phase linear predictive filtering [17, 21]. In linear predictive filtering, a given sample in a data set is assumed to be a linear combination of M previous samples. A modified zero-phase whitening filter is constructed by zero-padding the initial filter, converting to the frequency domain and correcting for dispersion in order to avoid introducing phase errors [19].

QPipeline is based on the Q transform, wherein the time series $s(t)$ is projected onto complex exponentials with bisquare windows, defined by central time τ, central frequency f_0 and quality factor *Q* (approximately the number of cycles present in the waveform). This can be represented by the formula

$$\begin{aligned} X(\tau, f_0, Q) \;=\; & \int_{-\infty}^{+\infty} \tilde{s}(f) \left(\tfrac{315}{128\sqrt{5.5}} \tfrac{Q}{f_0}\right)^{1/2} \\ & \left[1 - (\tfrac{fQ}{f_0\sqrt{5.5}})^2\right]^2 e^{+i2\pi f\tau} df. \end{aligned} \tag{3.1}$$

Because it uses a set of generic complex exponentials as a template bank, QPipeline thus functions much like a matched filter search for waveforms which appear as sinusoidal Gaussians after the data stream is whitened [17] . This bank of templates is tiled logarithmically in Q and frequency, but tiles at a given frequency are spaced linearly in time. The templates are spaced in such a way that we lose no more than 20% of the trigger's normalized energy due to mismatches δt, δf and δQ [19].

The significance of a trigger is expressed in terms of its normalized energy Z, defined by taking the ratio of the squared projection magnitude to the mean squared projection magnitude of other templates at the same Q and frequency:

$$Z = |X|^2 / \langle |X|^2 \rangle \,. \tag{3.2}$$

A gravitational wave signal would appear identical (in units of calibrated strain) in the colocated, co-aligned H1 and H2 detectors at the Hanford site. Therefore, a new *coherent* data stream is formed from the noise-weighted sum of the two data streams. Mathematically, this can be expressed as:

$$\tilde{s}_{H+} = (\frac{1}{S_{\rm H1}} + \frac{1}{S_{\rm H2}})^{-1} (\frac{\tilde{s}_{\rm H1}(f)}{S_{\rm H1}} + \frac{\tilde{s}_{\rm H2}(f)}{S_{\rm H2}}) \tag{3.3}$$

where $S_{\rm H1}$ and $S_{\rm H2}$ are the power spectral densities of the two interferometers and $\tilde{s}_{\rm H2}(f)$ and $\tilde{s}_{\rm H1}(f)$ are the frequency domain representation of the strain data coming from H1 and H2.

The coherent analysis also defines a *null* stream, H_-, which is just the normalized difference between the strain data of H1 and H2. For lower frequency analyses, if the null H_- stream value is too large the coherent H_+ stream is vetoed at the corresponding time [19]. This is because a signal with consistent magnitude in both detectors should cancel out to zero, so a large null stream value indicates an inconsistent signal detected by the two interferometers. However, we do not apply this null stream consistency veto in the high frequency search and simply take the result of the coherent stream as the final QPipeline result for the Hanford site, leaving this consistency test as part of the follow-up procedure to vet any gravitational wave candidates. This is for two reasons: a.) at the time the analysis was designed it was feared that substantially larger systematic uncertainties in calibration at higher frequencies mean that the criterion for what constitutes *consistent* behavior between the two Hanford detectors would have to have been substantially relaxed, and b.) a smoother, less glitchy background population makes this consistency test only marginally useful (less than a 1% reduction in the clustered coincident background trigger rate) above 1 kHz in any case.

For this analysis, we threshold at a normalized energy $Z = 16$ for both sites. Along with CorrPower Γ (defined in section III E) this is one of the variables used to tune the false alarm rate of the analysis. In the case of Livingston, Z is simply the normalized energy coming out of the Q transform, whereas in the case of Hanford, this is the normalized energy coming out of the coherent stream.

While lower frequency data are analyzed at 4096 Hz to save on computational costs, this search needs the full LIGO rate of 16384 Hz in order to analyze higher frequencies. This higher sampling rate required computational tradeoffs relative to lower frequency analysis. Specifically, data were analyzed in blocks of 16 seconds rather than 64 seconds due to memory constraints. Additionally, the templates applied covered signals with *Q* from 2.8 to 22.6 rather than extending to higher *Q*s in order to reduce the required processing time. This choice of *Q* range is consistent with theoretical predictions, since the models under study in this frequency range generally predict signals of a few cycles. More detailed information on QPipeline can be found in [19] and [17].

B. Post-Processing of Triggers

After triggers have been identified at both sites, the two lists are combined into one coincident trigger list. In order to form

a coincident trigger, there must be triggers at both sites which have time and frequency values consistent with each other. Specifically, the peak times τ_H and τ_L at the Hanford and Livingston sites must satisfy the inequality

$$|\tau_H - \tau_L| < \max(\delta\tau_H, \delta\tau_L)/2 + 20\ \mathrm{ms} \qquad (3.4)$$

where $\delta\tau_H$ and $\delta\tau_L$ are the durations of the two triggers. The time of flight for a gravitational wave traveling directly between the detectors is approximately 10 ms, so a 20 ms coincidence window is somewhat padded to allow for misreconstructions in the central time of the waveform. This is a more conservative window choice than that of the corresponding QPipeline S5 all-sky burst search at lower frequencies [19], but the difference in the coincidence window has minimal effect on the sensitivity of the analysis.

Similarly, the central frequencies $f_{0,H}$ and $f_{0,L}$ of the two triggers must satisfy the condition:

$$|f_{0,H} - f_{0,L}| < \max(\delta f_{0,H}, \delta f_{0,L})/2. \qquad (3.5)$$

where $\delta f_{0,H}$ and $\delta f_{0,L}$ are the bandwidths of the triggers at the two sites. This definition is identical to that used in the lower frequency analysis.

Once this coincident list has been obtained, the coincident triggers are clustered in periods of 1 second, taking only the trigger with the highest normalized energy, in order to eliminate multiple triggers from the same feature in the data stream. The remaining downselected triggers are referred to as *clustered triggers*.

C. Data Quality Cuts

Data quality cuts are designed to remove periods of data during which there is an unusually high rate of false triggers due to known causes. An effective data quality cut should remove a large number of spurious background triggers while resulting in a relatively small reduction in the livetime of the analysis. These cuts are selected from a predetermined set of data quality *flags*, which identify times in which environmental monitors suggest a disturbance that might influence the gravitational-wave readout. We use the same *category 1* and *category 2* data quality cuts as the S5 low frequency burst searches [19]. Category 1 cuts remove periods of time where there were major, obvious problems, such as a calibration line dropout or the presence of hardware injections, which make the data unusable. Similarly, category 2 cuts remove periods for which there is a clear external disturbance which distorts the data. Category 2 cuts result in a loss of 1.4% of the triple-coincident livetime. While category 1 periods are removed before the start of the analysis, category 2 periods are removed at a later stage so as to avoid creating a large number of very short science segments which are impractical to process using QPipeline.

Category 3 data quality flags, which define periods where the data are analyzable but still somewhat suspect due to some known cause, were studied one at a time for their effectiveness relative to high frequency triggers. The category 3 flags used for this high frequency analysis are a subset of those adopted at low frequencies. Flags which removed QPipeline background triggers at a much higher rate than expected by random Poisson coincidence were selected for use. Specifically, the rate of clustered triggers must be at least 1.7 times higher for periods when a given data quality flag is on relative to periods when that flag is off. As in the lower frequency analyses, category 3 data quality flags are used only for purposes of setting the upper limit, but triggers surviving to the end of the pipeline may still be examined as gravitational wave event candidates if they are within a category 3 data quality segment. The flags used in this high frequency analysis are summarized in Table I. Applying the selected category 3 data quality flags ultimately removes 19.4% of the surviving coincident time-shifted background triggers and results in a 1.7% reduction in triple coincident livetime.

D. Auxiliary Channel Vetoes

The LIGO interferometers use a large set of auxiliary detectors to determine when potential event candidates are the result of environmental causes (such as seismic activity or electromagnetic interference) or problems with the interferometer itself rather than actual gravitational waves. Triggers from these auxiliary detectors act as *vetoes*, removing potential gravitational wave candidate events that occur at the same time as the trigger in the auxiliary detector. These vetoes are distinguished from the data quality cuts described in the previous section because they are determined in a statistical way and remove triggers from a much shorter period of time (tens to hundreds of milliseconds around a particular veto trigger rather than blocks of seconds to thousands of seconds in the case of data quality cuts). Vetoes are divided into categories using the same definitions as data quality flags. The same list of category 2 vetoes used at low frequencies [19] was applied to this search. These vetoes require multiple magnetometer or seismic channels at a given site to be firing simultaneously.

This analysis also uses the same method of selecting which category 3 auxiliary channel vetoes to apply as was used for the lower frequency S5 all-sky searches, but used an independent set of high frequency QPipeline time-shifted background triggers to select these vetoes. A list of potential vetoes is assembled from the various auxiliary channels at different thresholds and with different coincidence windows. The effectiveness of each potential veto is measured by its efficiency-to-deadtime ratio, which is the percentage of background triggers it removes from the analysis divided by the percentage of the total livetime it removes. The vetoes which are actually applied are selected in a hierarchical fashion, first picking the most effective veto, then calculating the effectiveness of the remaining possible vetoes after this one has been applied. The next most effective veto is then selected and the process repeated until all remaining veto candidates have either an efficiency-to-deadtime ratio less than 3 or a probability of their effect resulting from random Poisson coincidence

TABLE I: Category 3 data quality cuts for high frequency analysis.

Flag name	Description	Livetime Loss (s)	Ratio of Clustered Trigger Rate (Flag On:Flag Off)
H1:WIND_OVER_30MPH	Heavy wind at ends of H1 arms	5531	1.93
H1:DARM_09_11_DHZ_HIGHTHRESH	Up-conversion of seismic noise at 0.9 to 1.1 Hz	6574	1.76
H1:SIDECOIL_ETMX_RMS_6HZ	Saturation of side coil current in H1 X end mirror	1360	2.11
H1:LIGHTDIP_02_PERCENT	Significant dip in stored laser light power in H1	34336	2.24
H2:LIGHTDIP_04_PERCENT	Significant dip in stored laser light power in H2	40562	2.04
L1:LIGHTDIP_04_PERCENT	Significant dip in stored laser light power in L1	115584	2.85
L1:BADRANGE_GLITCHINESS	Abrupt drop in interferometer sensitivity, quantified in terms of effective range for inspiral signals	3185	1.95
L1:HURRICANE_GLITCHINESS	Hurricane was active near Livingston	42917	2.92

greater than 10^{-5}. The vetoes were selected using a set of background triggers obtained from 100 time-shifts of L1 with respect to H1H2, with offsets ranging from -186 to 186 seconds in increments of 3 seconds. Time-shifts which were also divisible by 5 and thus present in the set used to determine the final background of the analysis were omitted, making the veto training and test sets independent. Of 18831 triggers remaining in time-shifted background after category 3 data quality cuts, 2284 are removed by vetoes (12% efficiency), while the vetoes cause a 2% reduction in the overall livetime of the analysis.

E. Cross-Correlation Test with CorrPower

The remaining clustered triggers are next subjected to cross-correlation consistency tests using the program CorrPower [22]. CorrPower has previously been used in S3 and S4 analyses [2, 5]. Unlike QPipeline, which only looks for excess power on a site-by-site basis, CorrPower thresholds on normalized correlation between data streams in different detectors. CorrPower was selected for use in this analysis because it is relatively fast computationally and effective for roughly co-aligned interferometers such as LIGO. For analyses including detectors with substantially different alignments relative to LIGO, such as Virgo or GEO 600, one does not necessarily obtain consistent correlated signals between interferometers and more sophisticated fully coherent techniques such as Coherent WaveBurst [23] or X-pipeline [24] would be preferable.

Before applying the correlation test, data was filtered to the 1–6 kHz target frequency range of the search. Additionally, triggers were rejected entirely if their central frequency as determined by QPipeline was greater than 6 kHz. Since this analysis extends CorrPower to higher frequency regimes compared to previous analyses, it was necessary to add $Q = 400$ notch filters at frequencies of 3727.0, 3733.7, 5470.0 and 5479.2 Hz, which correspond to "butterfly" and "drumhead" resonant frequencies of the interferometers' optical components. The data are whitened. CorrPower then measures correlation using Pearson's linear correlation statistic:

$$r = \frac{\sum_{i=1}^{N}(x_i - \bar{x})(y_i - \bar{y})}{\sqrt{\sum_{i=1}^{N}(x_i - \bar{x})}\sqrt{\sum_{i=1}^{N}(y_i - \bar{y})^2}} \qquad (3.6)$$

where x and y are in this case the time series being compared for the two interferometers, $\bar{x}$ and $\bar{y}$ are the average values and N is the number of samples within the window used for the calculation. This *r-statistic* is calculated over windows of duration 10, 25 and 50 ms. This variable is maximized over various time-shifts between the two interferometers. The maximum time-shift between one of the Hanford detectors with the detector at Livingston is 11 ms, whereas the maximum time-shift between the two Hanford detectors is 1 ms. The final output of CorrPower which we use as a data selection criterion is called Γ. Γ is an average of the r-statistic values for each of the 3 detector combinations, using the integration length and relative time-shift between interferometers which results in the highest overall r-statistic value.

F. Tuning for the Final Cut

CorrPower was run on the triggers resulting from the 100 background time-shifts. This distribution was used to deter-

mine the value of the cut on the CorrPower Γ output variable. In order to obtain an estimated false alarm rate (FAR) of around one tenth of an event candidate in the analysis of time-shift-free foreground data, cuts were applied to remove the bulk of the time-shifted background distribution, only keeping triggers with Γ values greater than 6.2 and a Qpipeline normalized energy greater than $Z = 16$ at both sites. This results in a final false alarm rate of $\sim 10^{-8}$ Hz.

IV. PROPERTIES OF LIGO DATA ABOVE 1 KHZ

A. High Frequency Trigger Distributions

Although the sensitivity of the detector is poorer at higher frequencies, the noise is more stationary in the shot-noise dominated regime. QPipeline normalized energy distributions from H1H2 for both high (>1 kHz) and low (<1 kHz) frequency triggers are shown for a single day (December 11th, 2005) in Figure 3. The distribution of single interferometer triggers at higher frequencies falls off substantially more sharply than does the lower frequency distribution and contains far fewer statistical outliers. The poorer statistics of the low frequency data set are due to glitches in the band below 200 Hz.

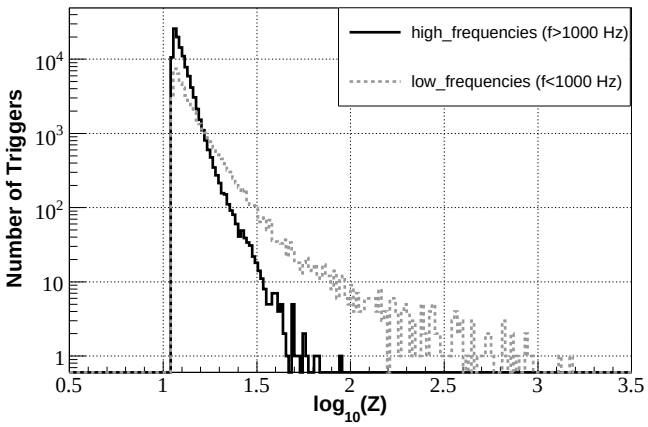

FIG. 3: Normalized energy Z of high and low frequency QPipeline triggers. The low frequency distribution contains a substantially higher number of outliers.

B. Systematic Uncertainties

Due to variations in the response of the detectors as a function of frequency, systematic uncertainties are calculated separately for each of three detection bands: below 2 kHz, 2 to 4 kHz and 4 to 6 kHz. The dominant source of systematic uncertainties is from the amplitude measurements in the frequency domain calibration. The individual amplitude uncertainties from each interferometer – of order 10% – are combined into a single uncertainty by calculating a combined root-sum-square amplitude SNR and propagating the individual uncertainties in this equation assuming each error is independent. In addition to this primary uncertainty, there is a small uncertainty (3.4% or less depending on frequency band) introduced by converting from the frequency domain to the time domain strain series on which the analysis was actually run [20].

There is also phase uncertainty on the order of a few degrees in each interferometer and in each frequency band, arising both from the initial frequency domain calibration and the conversion to the time domain. However, phase uncertainties are within acceptable tolerance. In this analysis in particular, the omission of the null stream in QPipeline means the analysis is generally insensitive to phase shifts between the interferometers on the order of those observed. Likewise, CorrPower is mostly insensitive to phase shifts between interferometers because it automatically maximizes over multiple time-shifts between the interferometers and will therefore still find the maximum possible correlation. Some distortion in the shape of broadband signals due to differing phase response at different frequencies is in principle possible. However, this is not a significant concern since the phase uncertainties at all frequencies correspond to phase shifts on the order of less half a sample duration. We therefore do not make any adjustment to the overall systematic uncertainties due to phase error.

The antenna pattern for LIGO is normally calculated using the long wavelength approximation, which assumes the period of oscillation of a gravitational wave is large with respect to the transit time of a photon down the length of the interferometer arm and back. This assumption is less accurate as the frequency increases. However, comparing results using the approximate long wavelength antenna pattern and frequency-dependent exact antenna pattern [26] even towards the extreme high end of our frequency range (at 6 kHz) results in sensitivity calculations (see next section) differing by only $\sim$1%. Thus, the approximation of a constant antenna pattern has a negligible effect on the analysis. Finally, we include a statistical uncertainty of around 2.7% (with some variation from waveform to waveform due to different numbers of injected waveforms).

In each frequency band the frequency domain amplitude uncertainties are added in quadrature with the other smaller uncertainties to obtain the total uncertainty. The total 1 σ uncertainties are then scaled by a factor of 1.28 to obtain the factor by which our $h_{\rm rss}$ limits are rescaled in order to obtain values consistent with 90% confidence level upper limits. These net uncertainty values are 11.1% in the less than 2 kHz band, 12.8% in the 2-4 kHz band and 17.2% in the 4-6 kHz band. Waveforms with significant signal content in multiple bands are considered to be in the band with the larger uncertainty.

V. DETECTION EFFICIENCY

Efficiency curves have been produced for three types of signal. The cuts were developed on a set of 15 linearly polarized Gaussian-enveloped sine waves (sine-Gaussians) of the form

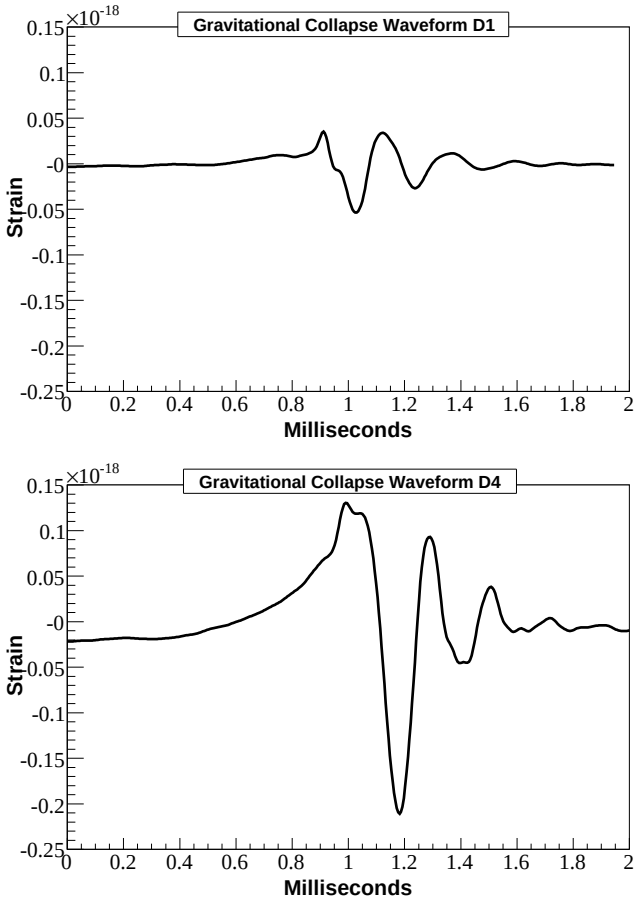

FIG. 4: Two example high frequency waveforms resulting from gravitational collapse of rotating neutron star models [9]. D1 results from a nearly spherical 1.26 solar mass star while D4 results from the collapse of a maximally deformed 1.86 solar mass star into a black hole. The figures show the plus polarization for each waveform (the cross polarization is at least an order of magnitude weaker in both cases) at a distance of 1 kpc, assuming optimal sky location and orientation. At this distance, the $h_{\rm rss}$ magnitudes of the two waveforms are $5.7 \times 10^{-22}{\rm Hz}^{-1/2}$ for D1 and $2.5 \times 10^{-21}{\rm Hz}^{-1/2}$ for D4. They differ from the figures presented in [9] in that the non-physical content at the beginning of the simulations has been removed.

$$h\left(t_0+t\right) = h_0 \sin\left(2\pi f_0 t\right) \exp\left(-\left(2\pi f_0 t\right)^2/2Q^2\right) \quad (5.1)$$

where f_0 and t_0 are the central frequency and time of the waveform and Q is the quality factor defined previously. Additionally, we tested a set of three linearly polarized Gaussian waveforms as well as two waveforms taken from simulations by Baiotti *et al*. [9], which models gravitational wave emission from neutron star gravitational collapse and the ringdown of the subsequently formed black hole using polytropes deformed by rotation. The two scenarios studied here are designated D1, a nearly spherical 1.26 solar mass star, and D4, a 1.86 solar mass star that is maximally deformed at the time of its collapse into a black hole. These two waveforms are shown in Figure 4. These two specific waveforms represent the extremes of the parameter space in mass and spin considered by Baiotti *et al*.

The BurstMDC and GravEn packages [27] were used to create simulated gravitational-wave "injections" which were superimposed on real data in a semi-random way at intervals of approximately 100 seconds. This placed all injections far enough apart that whitening and noise estimation using data surrounding one injection is never affected by a neighboring injection. Each waveform was simulated between 1000 and 1200 times for each of the 18 different amplitudes. The intrinsic amplitude of a gravitational wave at the Earth, without folding in antenna response factors, is defined in terms of its root-sum-squared strain amplitude:

$$h_{\rm rss} \equiv \sqrt{\int \left(|h_+\left(t\right)|^2 + |h_\times\left(t\right)|^2\right){\rm dt}} \quad (5.2)$$

where $h_+\left(t\right)$ and $h_\times\left(t\right)$ are the plus and cross-polarization strain functions of the wave. Since h is a dimensionless quantity, $h_{\rm rss}$ is given in units of ${\rm Hz}^{-1/2}$.

The injections were distributed isotropically over the sky. Thus, even a few nominally very strong software injections are missed by the pipeline because they are oriented in a very sub-optimal way relative to at least one interferometer. Since they are simulating an actual astrophysical system, the D1 and D4 waveforms also include a randomized source inclination in addition to random sky location and polarization. A $\sin^2(\iota)$ dependence on the inclination angle was assumed. Figure 5 shows efficiency curves for some of these waveforms as a function of signal amplitude. The $h_{\rm rss}$ values for which 50% and 90% of sine-Gaussian injections are detected are summarized in Table II. Figure 6 shows the detection efficiency for the simulated D1 and D4 Baiotti *et al*. models as a function of distance from Earth, indicating that a neutron star collapse would have to happen nearby (within a kiloparsec) to be detectable at our current sensitivity.

Hardware injections, wherein actuators were used to physically simulate a gravitational wave in the interferometers by moving the optical components, were performed throughout S5. Although the numbers and variety of amplitudes were not sufficient to produce hardware injection efficiency curves, sine-Gaussian hardware injections at 1304, 2000 and 3067 Hz were reliably recovered using the high frequency search pipeline at amplitudes large enough that their detection is expected based on sensitivities determined by software injection efficiencies. Table III shows the central frequency, amplitude and fraction of hardware injections detected. For hardware injections, amplitude is given in terms of $h_{\rm rss,det}$, the root sum square of the strain in the detector. This is defined analogously to equation 5.2, with $h_{+,\rm det}$ and $h_{\times,\rm det}$ in place of h_+ and $h_\times$.

Good timing and frequency reconstruction help improve detection efficiency. Using $Q = 9$ sine-Gaussian waveforms, the timing resolution has been demonstrated to be within one cycle of the waveform and frequency resolution is better than 10%, limited by the coarseness in frequency space of the templates used in QPipeline.

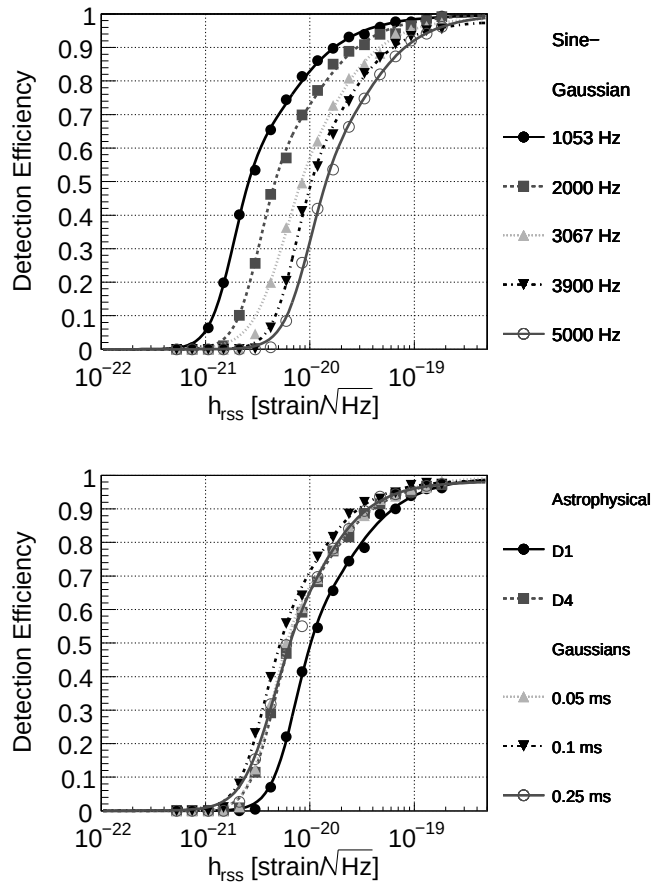

FIG. 5: Software injection efficiency curves for the set of sine-Gaussians of various frequencies (top) and Gaussians plus astrophysical waveforms (bottom). There is a consistent reduction in efficiency as a function of frequency following the noise distribution.

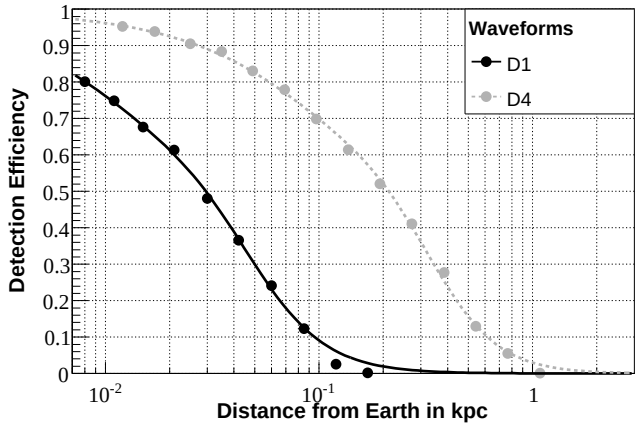

FIG. 6: Efficiency as a function of distance from Earth for supernova collapse waveforms D1 and D4 [9], assuming random sky location, polarization and inclination angle ι. A $\sin^2(\iota)$ dependence on the inclination angle was assumed.

TABLE II: $h_{\rm rss}^{50\%}$ and $h_{\rm rss}^{90\%}$ values (the root sum square strain at which 50% or 90% of injections are detected) for $Q = 9$ sine-Gaussians. Values in this table are adjusted for systematic uncertainties as described in section IV B.

Central Frequency	$h_{\rm rss}^{50\%}$ (Hz$^{-1/2}$)	$h_{\rm rss}^{90\%}$ (Hz$^{-1/2}$)
1053	2.87×10^{-21}	1.97×10^{-20}
1172	3.15×10^{-21}	2.04×10^{-20}
1304	3.31×10^{-21}	2.06×10^{-20}
1451	3.73×10^{-21}	2.33×10^{-20}
1615	3.99×10^{-21}	2.67×10^{-20}
1797	4.91×10^{-21}	3.10×10^{-20}
2000	5.22×10^{-21}	3.30×10^{-20}
2226	6.08×10^{-21}	3.74×10^{-20}
2477	6.63×10^{-21}	4.47×10^{-20}
2756	7.59×10^{-21}	5.14×10^{-20}
3067	9.20×10^{-21}	5.62×10^{-20}
3799	1.17×10^{-20}	8.06×10^{-20}
3900	1.19×10^{-20}	7.87×10^{-20}
5000	1.67×10^{-20}	9.47×10^{-20}

TABLE III: S5 $Q = 9$ sine-Gaussian hardware injections above 1 kHz. Note that $h_{\rm rss,det}$ and $h_{\rm rss}$ are different quantities because $h_{\rm rss}$ does not include a sky location dependent antenna response factor, which will reduce the detector response by an additional factor of 0.38 on average. Care should therefore be taken when comparing to Table I.

Central Frequency (Hz)	$h_{\rm rss,det}$ (Hz$^{-1/2}$)	fraction recovered
1304	5.00×10^{-22}	0/2
1304	1.28×10^{-20}	16/16
1304	2.56×10^{-20}	16/16
2000	6.00×10^{-22}	0/102
2000	1.00×10^{-21}	0/4
2000	1.20×10^{-21}	14/127
2000	2.40×10^{-21}	125/125
2000	4.80×10^{-21}	117/117
2000	9.60×10^{-21}	21/21
2000	1.92×10^{-20}	16/16
2000	3.84×10^{-20}	16/16
3067	7.21×10^{-21}	13/13
3067	1.44×10^{-20}	13/13
3067	2.88×10^{-20}	3/3
3067	5.76×10^{-20}	3/3

VI. RESULTS

Having tuned the analysis on background from 100 time-shifts and tested it on a single day of data, we then performed the analysis on the actual coincident (or "foreground") data. No event candidates above our threshold were observed.

As in previous burst analyses (e.g. [2]), we set single-sided frequentist upper limits on the rate of gravitational wave emis-

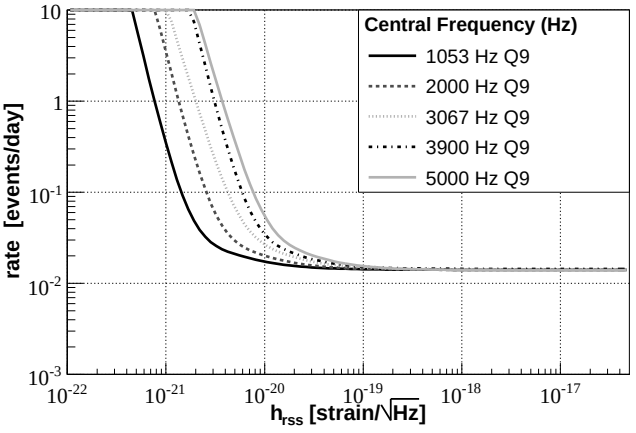

FIG. 7: Upper limit curves for a number of our tested waveforms. The rate at Earth of gravitational waves of each given type is excluded at a 90% confidence level. The curves have been adjusted to account for systematic uncertainties as described in section IV B.

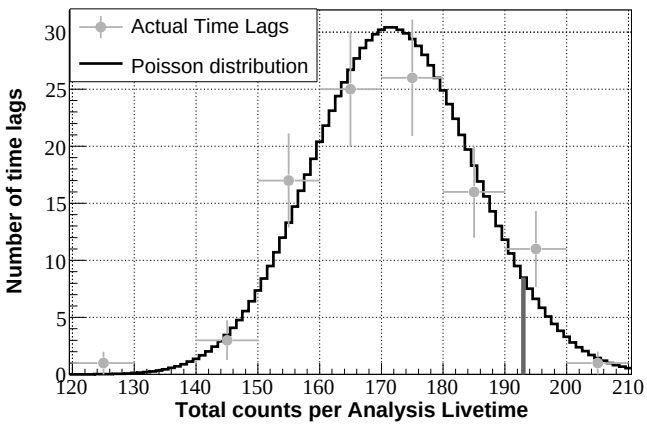

FIG. 8: Histogram showing number of time-shifts vs. counts normalized to analysis livetime. Superimposed is the expected distribution based on Poissonian statistics, which is consistent with the observed distribution. The black line at 193 counts indicates the actual number of foreground triggers observed.

TABLE IV: Number of triggers surviving various stages of the analysis: initial coincident triggers, triggers remaining after the removal of segments removed due to data quality criteria, triggers remaining after vetoes based on auxiliary channels have been applied and triggers ultimately surviving after the CorrPower linear correlation cut (Γ). Shown are results for 100 time-shifts, the same result normalized to the actual livetime, and the foreground results from the analysis performed without time-shifting the data. The background normalization reflects the fact that the livetime is different for different time-shifts.

	Background Count	Normalized Background	Unshifted Count
Coincident triggers	23361	242.9	265
After data quality cuts	18831	195.8	223
After auxiliary channel vetoes	16547	172.0	193
After Γ >6.2 threshold	11	0.115	0

sion. The upper limits in the frequency range 1–6 kHz are shown in Figure 7 for a sub-sample of our tested waveforms. 161.3 days of triple-coincident livetime were analyzed. After performing category 3 data quality cuts and vetoes, 155.5 days of triple-coincident data were used to set upper limits on gravitational wave emission. For gravitational waves with amplitudes such that detection efficiency approaches 100%, the upper limit asymptotically approaches a value of 0.015 events per day (5.4 events per year), as determined primarily by the livetime of the analysis.

The number of triggers surviving through each stage of the analysis are shown in Table IV. While there are no event candidates above our threshold in this analysis, the rates before the final CorrPower cut are slightly higher than expected. However, assuming Poissonian statistics, this is not a statistically significant excess since there is a 6.2% chance of getting at least the observed 193 foreground triggers after all data quality cuts and vetoes have been applied. Figure 8 demonstrates that the rate of triggers per time-shift can in fact be treated as a Poisson distribution.

The foreground to background consistency of the CorrPower Γ distribution (Fig. 9) and QPipeline normalized energies from the Livingston and Hanford sites (Fig. 10) were also studied. These plots are produced after all data quality cuts and vetoes were applied, but before the final CorrPower Γ cut. The distributions are plotted cumulatively, i.e. each bin shows foreground and time-shifted background counts greater than or equal to the marked value. Other than the upward fluctuation in total counts already discussed, the distributions themselves are essentially consistent with expectation.

Since they appeared to stand out slightly from the expected background distribution (although not at a statistically significant level), the loudest 3 triggers in Hanford QPipeline normalized energy, loudest 2 triggers in Livingston normalized energy and the trigger with highest CorrPower Γ value were studied on an individual basis using Qscan [17]. All of the triggers appear consistent with the background population. In most cases the triggers arise from the correlation of a fairly loud trigger with what appears to be one of a population of glitches of smaller magnitude in the other interferometers.

In addition to the previously described search requiring data from all 3 LIGO interferometers, we also performed a check for interesting events during times in which H1 and H2 science quality data were available, but L1 data was not. The two-detector search is less sensitive than the three-detector search and background estimation is less reliable, so we do not use this data when setting upper limits. However, in the first calendar year of S5, there are 77.2 days of livetime with only H1 and H2 data available (roughly half the livetime with simultaneous data from all three interferometers), so it is worth checking this data for potential gravitational wave candidates. This check used procedures similar to the analy-

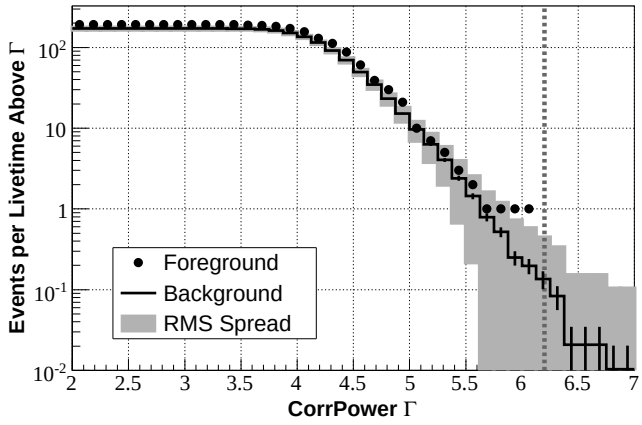

FIG. 9: CorrPower Γ distribution for background (normalized to the livetime of the analysis) and foreground distributions before the final CorrPower cut. The gray region is the RMS spread of counts in the background time-shifts while the error bars are the error in the mean counts per time-shift. The dotted line shows the cut at Γ=6.2.

sis previously described, including identical data quality and veto procedures.

Due to the presence of correlated transients in H1H2 data, performing time-shifts of one detector relative to the other is not a reliable means of obtaining an accurate background. Instead, we use the unshifted H1H2 coincident triggers from the H1H2L1 analysis as our estimate of the background since we have already determined that there are no gravitational wave candidates in this data set. However, the H1H2L1 data set is only about twice the livetime of the H1H2-only data set, so we are required to extrapolate the false alarm probability distribution to obtained the desired false alarm rate. To compensate for the uncertainties in our estimate of the false alarm probability introduced by the reduced data set and the extrapolation, we target a more conservative false alarm probability of $\sim$0.01 triggers for the H1H2-only analysis. This lower false alarm probability and the lack of L1 coincidence as a veto requires stricter cuts, specifically coherent energy $Z > 100$ from QPipeline and $\Gamma > 10.1$ from CorrPower. As in the three-detector search, there were no events above threshold (see Fig. 11) upon examination of the zero-lag foreground data, thus no potential gravitational wave candidates were identified in the two-detector search.

VII. SUMMARY AND FUTURE DIRECTIONS

We have searched the few-kilohertz frequency regime for gravitational wave signals using the first calendar year of LIGO's fifth science run. No gravitational wave events were identified, and we have placed upper limits on the emission of gravitational waves in this frequency regime.

The second calendar year of S5 remains to be analyzed in this frequency range. Several months of this run overlap with the first science run of the Virgo [16] detector, which began

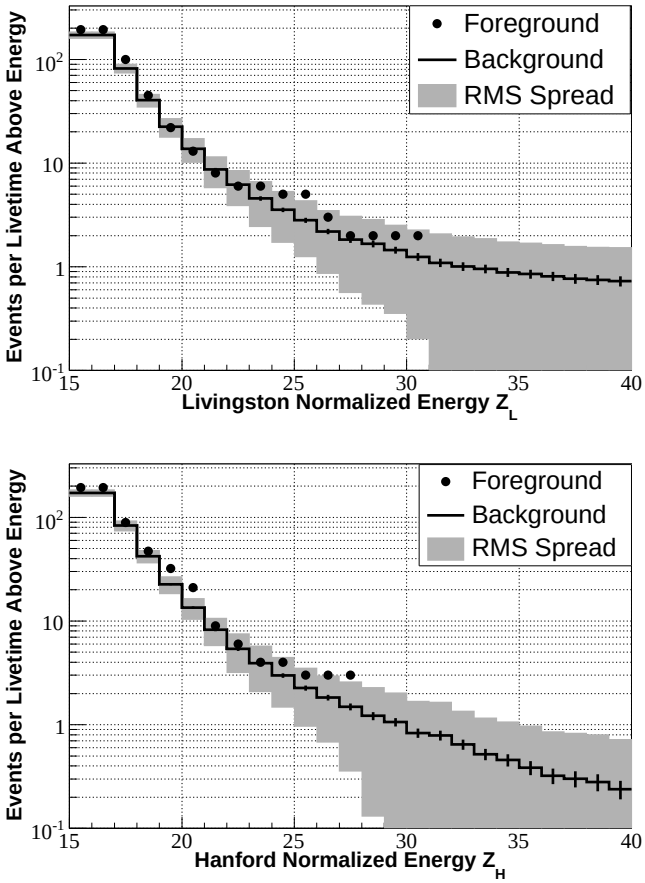

FIG. 10: QPipeline significance distribution for background (normalized to the livetime of the analysis) and foreground distributions at the Livingston (top) and Hanford (bottom) sites before the final CorrPower cut. The gray region is the RMS spread of counts in the background time-shifts while the error bars are the error in the mean counts per time-shift.

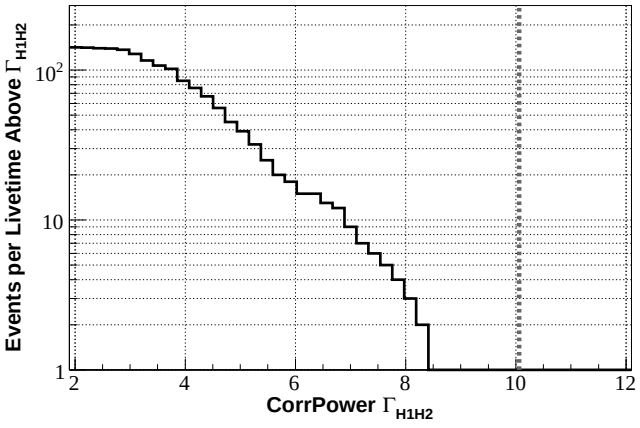

FIG. 11: CorrPower Gamma zero-lag distribution for the H1H2 analysis. The dotted line shows the cut at Γ=10.1.

on May 18th, 2007. During this period of overlap, data from Virgo as well as the LIGO interferometers will be incorporated into high frequency analysis. Since Virgo is not coaligned with the LIGO detectors, this will require fully coherent analysis tools rather than CorrPower. Above 1 kHz Virgo and LIGO have comparable sensitivities, making their combination especially advantageous in the few-kilohertz regime.

The next LIGO science run will be done with Enhanced LIGO [28], an improved version of the detectors. Most relevant to high frequency analysis, the dominant background of shot noise will be reduced by increasing the power of the laser from 10 W to $\sim$35 W, substantially improving the sensitivity of the detectors. Virgo+, a similarly enhanced version of Virgo, will operate simultaneously. After this, further improvements will lead to the AdvancedLIGO [29] and AdvancedVirgo [30] detectors coming online around 2014. Extending the analysis of gravitational wave data into the few-kilohertz regime will continue to be of scientific interest as these detectors become more and more sensitive.

Acknowledgments

The authors gratefully acknowledge the support of the United States National Science Foundation for the construction and operation of the LIGO Laboratory and the Science and Technology Facilities Council of the United Kingdom, the Max-Planck-Society, and the State of Niedersachsen/Germany for support of the construction and operation of the GEO 600 detector. The authors also gratefully acknowledge the support of the research by these agencies and by the Australian Research Council, the Council of Scientific and Industrial Research of India, the Istituto Nazionale di Fisica Nucleare of Italy, the Spanish Ministerio de Educación y Ciencia, the Conselleria d'Economia Hisenda i Innovació of the Govern de les Illes Balears, the Royal Society, the Scottish Funding Council, the Scottish Universities Physics Alliance, The National Aeronautics and Space Administration, the Carnegie Trust, the Leverhulme Trust, the David and Lucile Packard Foundation, the Research Corporation, and the Alfred P. Sloan Foundation. The authors thank Luca Baiotti and Luciano Rezzolla for providing simulation data and valuable discussion concerning the testing of astrophysical waveform models.

This document has been assigned LIGO Laboratory document number LIGO-P080080.

[1] D. Sigg for the LSC. Class. Quant. Grav. **23**, S51 (2006).
[2] B. Abbott *et al*, Class. Quant. Grav. **24**, 5343 (2007).
[3] B. Abbott *et al*, Phys. Rev. D **69**, 102001 (2004).
[4] B. Abbott *et al*, Phys. Rev. D **72**, 062001 (2005).
[5] B. Abbott *et al*, Class. Quant. Grav. **23**, S29 (2006).
[6] B. Abbott *et al*, Class. Quant. Grav. **25** 245008 (2008).
[7] C.D. Ott, Class. Quant. Grav. **26** 063001 (2009).
[8] L. Baiotti *et al*, Phys. Rev. Lett. **97**, 141101 (2006).
[9] L. Baiotti *et al*, Class. Quant. Grav. **24**, S187 (2007).
[10] R. Oechslin and H.-T. Janka, Phys. Rev. Lett. **99**, 121102 (2007).
[11] B.F. Schutz, Class. Quant. Grav. **16**, A131 (1999).
[12] J.G. Jernigan, AIP Conf. Proc. **586**, 805 (2001).
[13] K.T. Inoue and T. Tanaka, Phys.Rev.Lett. **91**, 021101 (2003).
[14] J.E. Horvath, Modern Physics Lett. A **20**, 2799 (2005).
[15] H.J. Mosquera Cuesta and D.M. Gonzalez, Phys. Rev. B **500**, 215 (2001).
[16] F. Acernese *et al* Class. Quant. Grav. **23**, S63 (2006).
[17] S. Chatterji, MIT Ph.D. thesis, September 2005.
[18] S. Chatterji *et al*, Class. Quant. Grav. **21**, S1809 (2004).
[19] B. Abbott *et al* (LSC), submitted to Phys. Rev D. gr-qc/0905.0020
[20] X. Siemens *et al*, Class. Quant. Grav. **21**, S1723 (2004).
[21] J. Makhoul, Proc. IEEE **63** (1975).
[22] L. Cadonati and S. Márka, Class. Quant. Grav. **22**, S1159 (2005).
[23] S. Klimenko *et al*, Class. Quant Grav. **25**, 114029 (2008).
[24] S. Chatterji *et al*, Phys. Rev. D **74**, 082005 (2006).
[25] S. Chatterji, L. Blackburn, G. Martin, and E. Katsavounidis, Class. Quant. Grav. **21**, S1809-18 (2004).
[26] M. Rakhmanov, J.D. Romano and J.T. Whelan, Class. Quant. Grav. **25**, 184017 (2008).
[27] A.L. Stuver and L.S. Finn, Class. Quant. Grav. **23**, S799 (2006).
[28] J.R. Smith *et al*, submitted to Class. Quant. Grav. gr-qc/0902.0381v2
[29] P. Fritschel *Gravitational-Wave Detection: Proc. SPIE* (2003) vol 4856 ed M. Cruise and P. Saulson (Bellingham, WA:SPIE Optical Engineering Press) pp 282-91.
[30] F. Acernese *et al* Class. Quant. Grav. **23**, S635 (2006).